Available online at www.sciencedirect.com
ScienceDirect
Trans. Nonferrous Met. Soc. China 22(2012) 404−410
Transactions of Nonferrous Metals Society of China
www.tnmsc.cn

Effect of configuration on magnetic field in cold crucible using for continuous melting and directional solidification

CHEN Rui-run, YANG Jie-ren, DING Hong-sheng, HUANG Feng, SU Yan-qing, GUO Jing-jie, FU Heng-zhi

School of Materials Science and Engineering, Harbin Institute of Technology, Harbin 150001, China

Received 10 October 2011; accepted 12 December 2011

Abstract: To improve the power efficiency and optimize the configuration of cold crucible using for continuous melting and directional solidification (DS), based on experimental verification, 3D finite element (FE) models with various configuration-elements were developed to investigate the magnetic field in cold crucible. Magnetic flux density (B) was measured and calculated under different configuration parameters. These parameters include the inner diameter (D_2), the slit width (d), the thickness of crucible wall, the section shape of the slit and the shield ring. The results show that the magnetic flux density in z direction (B_z) both at the slit and at the midpoint of segment will increase with the decrease of D_2 or with the increase of the width of the slit and the section area of wedge slit or removing the shield ring. In addition, there is a worst wall thickness that can induce the minimum B_z for a cold crucible with a certain outer diameter.

Key words: cold crucible; magnetic flux density; configuration design; directional solidification

1 Introduction

Electromagnetic cold crucible (EMCC) designed for continuous melting and directional solidification (DS) is an advanced technology for preparing refectory and reactive materials [1, 2]. One of its advantages is free or low contamination. EMCC is composed of a segmented copper crucible and an induction coil. In the process of continuous melting and directional solidification, the metal in cold crucible is heated to the liquid by an induction coil, and the new solidified ingot at the bottom continuously immerges into Ga−In liquid alloys for cooling, thus a high temperature gradient in perpendicular direction forms, which meets the requirement of DS.

In continuous melting and DS with EMCC, due to nonuniform distribution of electromagnetic force on the melt, the solid/liquid (S/L) interface is always curved [3], and thus the grain growth will be disturbed. Moreover, a low power efficiency of EMCC often results in an insufficient superheat degree of the melt, which will deteriorate the continuous growth of the grains. For these reasons, the main aims in designing the EMCC are to improve the distribution of the magnetic field and improve the power efficiency. Numerical method is exclusively applied to the EM simulation of cold crucible, and pervious investigations showed that the electromagnetic transparency and the power efficiency are determined by the cold crucible configuration [4−12]. However, the distribution of magnetic field in EMCC has not been fully comprehended, especially the magnetic flux density (B) at different positions at the same height. In addition, the 2D numerical model was adopted to calculate the magnetic flux density [13, 14]. However, there are some differences for the calculating results and experimental results. This shows that 2D numerical model is not ideal to investigate the effect of the configuration of cold crucible on the magnetic field. Therefore, in this study, based on experimental verification, a series of 3D FE models were systematically developed to calculate B to explore the effect of the configuration of cold crucible on the magnetic field. The commercial ANSYS program (distributed by ANSYS HIT) and self-developed FEM codes were applied.

2 Numerical tools and research method

2.1 FE model of cold crucible

The EMCC used for continuous melting and DS is cylindrical, with the height of 150 mm and 8 segments,

Foundation item: Project (2011CB605504) supported by the National Basic Research Program of China
Corresponding author: YANG Jie-ren; Tel: +86-451-86412394; E-mail: doudoubest@126.com
DOI: 10.1016/S1003-6326(11)61191-6

which was designed and fabricated by our group, as presented in Figs. 1(a) and (b). Based on this EMCC, the configuration parameters were changed, such as the inner diameter (D_2), the slit shape, the existence of shield ring (h_1, h_3), to calculate magnetic flux density in z direction (B_z) in EMCC using a 3D nodal-based method. The FE model of EMCC and its FE grids generation are shown in Fig. 2.

2.2 Governing equations in electromagnetic field

The cold crucible and the induction coil in EMCC system are considered the conductor, the eddy current mainly distributes in the skin layer, and the permeability of all materials is 1.0. Therefore, in the time-varying EM field under a lower frequency, Maxwell's equations are given as follows:

$$\nabla \times H = J \tag{1}$$

$$\nabla \times E = -\frac{\partial B}{\partial t} \tag{2}$$

$$\nabla \cdot B = \nabla \cdot (\nabla \times A) = 0 \tag{3}$$

where H is the magnetic field intensity; E is the electric field intensity; B is the magnetic flux density; A is the magnetic vector potential [15]. The magnetic field is a curl field, therefore the function of scalar potential cannot be used. However, no current exists in the free space (air), so H can be stated as a gradient of a scalar quantity:

$$H = -\nabla \cdot \Phi_{\mathrm{m}} \tag{4}$$

The magnetic scalar potential Φ_{m} has been adopted to save calculating memory and time. To solve A and Φ_{m}, the Alembert equation with dynamic potential function can be written as follows:

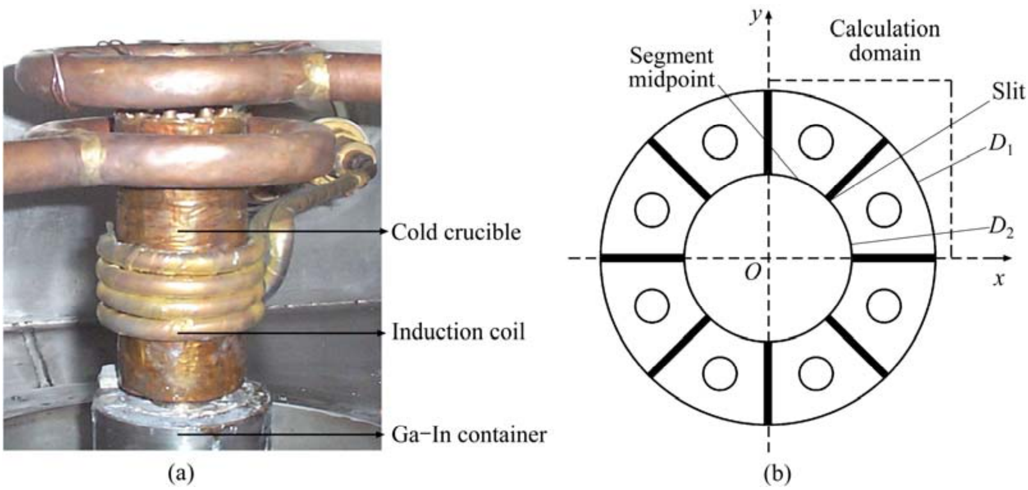

Fig.1 Bottomless type cold crucible (a) and its section (b)

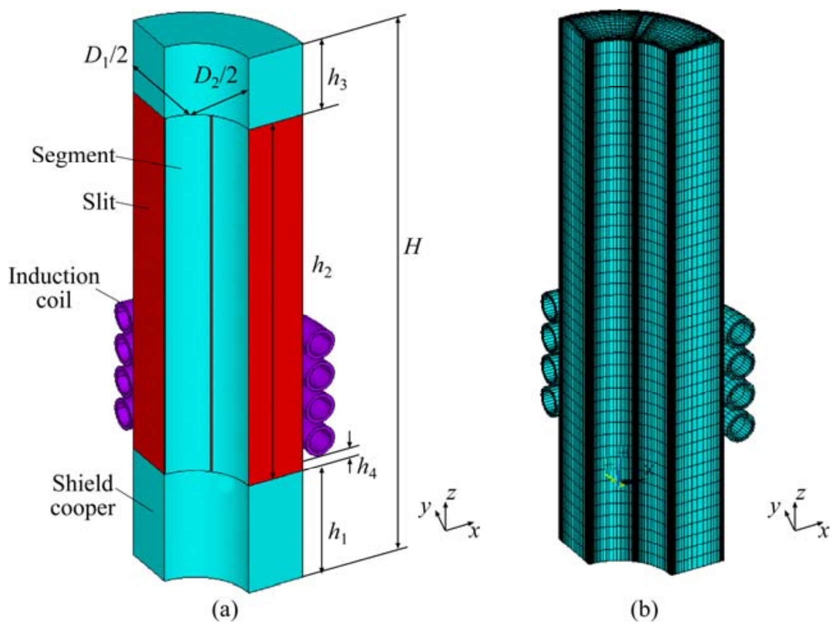

Fig. 2 Calculation model: (a) FE model; (b) FE grid

$$\nabla^2 \cdot A - \varepsilon\mu \frac{\partial^2 A}{\partial t^2} = -\mu J \tag{5}$$

$$\nabla^2 \cdot \Phi - \varepsilon\mu \frac{\partial^2 \Phi}{\partial t^2} = -\frac{\rho}{\varepsilon} \tag{6}$$

where ε is the permittivity. When the field sources J and ρ are given, A and $\Phi_{\rm m}$ can be solved and then substituting the solution into equations (2) and (3), B and E can be consequently solved [16].

2.3 Parameters of models

A standard crucible model is set and its geometry dimension is listed in Table 1, which includes the height of the nether and the upper shield rings (h_1 and h_3), the length of the slit (h_2), the height of the cold crucible (H), the outer and inner diameters of the cold crucible (D_1 and D_2), the induction coil position (h_1+h_4), the width (d) of the rectangular slit and the power parameters. In this study, each configuration element is individually changed, which is shown in Table 2, and the physical properties of the materials calculated in FE models are shown in Table 3.

Table 1 Dimensions and power parameters in standard crucible model

Configuration dimension/mm								Power parameter	
h_1	h_2	h_3	h_4	H	D_1	D_2	d	I/A	f/Hz
30	100	20	3	150	60	30	1	10^4	10^4

Table 2 Different levels of influence factors on magnetic field

Influence factor (variable)	Level
Inner diameter, D_2/mm	24, 30, 48
Wall thickness/mm	7, 9, 11, 13, 15, 17
Width of rectangular slit, d/mm	0.4, 0.8, 1.0, 1.2, 1.6

Table 3 Physical properties of materials used in FE models

Material	Resistivity/ ($10^{-8}\Omega\cdot$m)	Relative permeability
Induction coil	1.673	1
Cold crucible	1.8	1
Air		1

During induction heating process, the induced current on the metal mainly distributes in the skin layer due to skin effect, thus the magnetic field in EMCC which can be effectively utilized is near the crucible inner wall. For this reason, B_z at the slit and the midpoint of the segment on the inner wall are selected to explore the magnetic field distribution, which are noted in Fig. 1.

3 Results and discussion

3.1 Comparison between measured and calculated results

Considering the simplicity and the accuracy of experimental measurement, B_z at the cold crucible centre was measured in experiment and was calculated with 2D and 3D models respectively, the results are shown in Fig. 3 [17]. From this figure, the B_z calculated using a 2D model is slightly higher than that measured because the slit configuration and the shielding effect of the copper segment are omitted in this model. Whereas, the B_z calculated using a 3D model is in good agreement with the measured result. Therefore, the 3D numerical model can produce more accuracy result to reveal the distribution of the magnetic field in cold crucible. B_z under different configuration elements was calculated with 3D FE models.

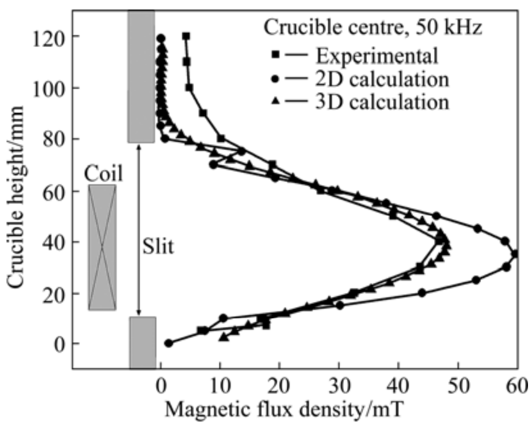

Fig. 3 Measured and calculated B_z at crucible center

3.2 Effect of configuration elements

3.2.1 Inner diameter of cold crucible

The inner diameter (D_2) of the crucible varies from 24 to 48 mm, and the thickness of the crucible wall keeps constant (15 mm). The results calculated under different D_2 are shown in Fig. 4. It can be seen from Fig. 4 that B_z increases with the decrease of D_2 in the height range of induction coil. This means that the reduced inner space of EMCC can increase the density of magnetic lines. Whereas, the results in Ref. [5] indicated that there is an optimal diameter with the maximum power efficiency. Therefore, undersized D_2 may cause lower energy utilization. By comparing B_z at the slit (Fig. 4(a)) with that at the segment midpoint (Fig. 4(b)) at the same height, B_z at slit is obviously higher than that at the segment midpoint, because the EM penetration is the strongest at the slit. The maximum of B_z appears near the half height of the induction coil. In addition, B_z will dramatically decrease when the position is out of the coil region.

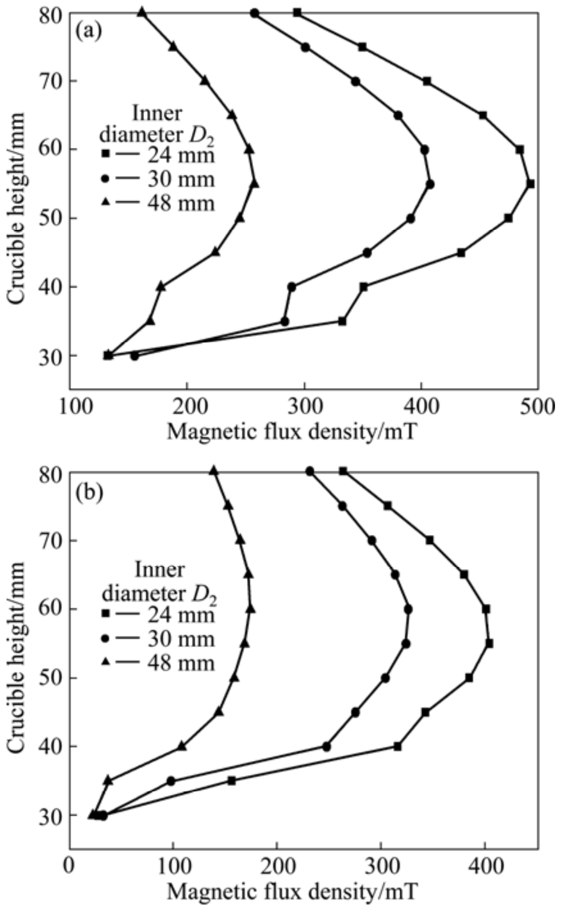

Fig. 4 B_z distribution under different D_2: (a) At slit; (b) At segment midpoint

3.2.2 Thickness of crucible wall

To investigate the effect of the wall thickness on B_z, the outer diameter D_1 (60 mm) keeps constant while the inner diameter D_2 is changed, the calculation results of B_z distribution at the slit and at the segment midpoint are shown in Figs. 5(a) and (b) and the maximum B_z at the slit and the segment midpoint are shown in Fig. 5(c).

When the wall thickness is changed from 7 to 17 mm, the maximum B_z both at the slit and the segment midpoint decreases initially till reaching the minimum value, and then increases, which are clearly presented in Fig. 5(c). A thinner copper wall can reduce the shielding effect caused by the crucible wall, which results in a higher B_z in EMCC, thus B_z decreases due to the slightly thickening of the crucible wall. Further, the crucible inner space reduces with the thickening of the crucible wall. As a consequence, the slit density on the crucible inner wall increases, therefore, B_z at the slit and at the segment will increase.

3.2.3 Width of rectangular slit

B_z was calculated when the slit width varied from 0.4 to 1.6 mm, the results are shown in Figs. 6(a) and (b) and the maximum values of them are shown in Fig. 6(c). It can be obviously seen from Figs. 6(a) and (b) that B_z increases with the extending of the slit width. B_z reaches the maximum value when the crucible height is about 55 mm, the maximum B_z and the slit width have a near linear relation, as shown in Fig. 6(c). Moreover, the extending of the slit width would improve the EM transparency, especially at the slit. Therefore, with the extending of the rectangular slit, the gap between the maximum B_z at the slit and that at the segment midpoint presents an expanding tendency.

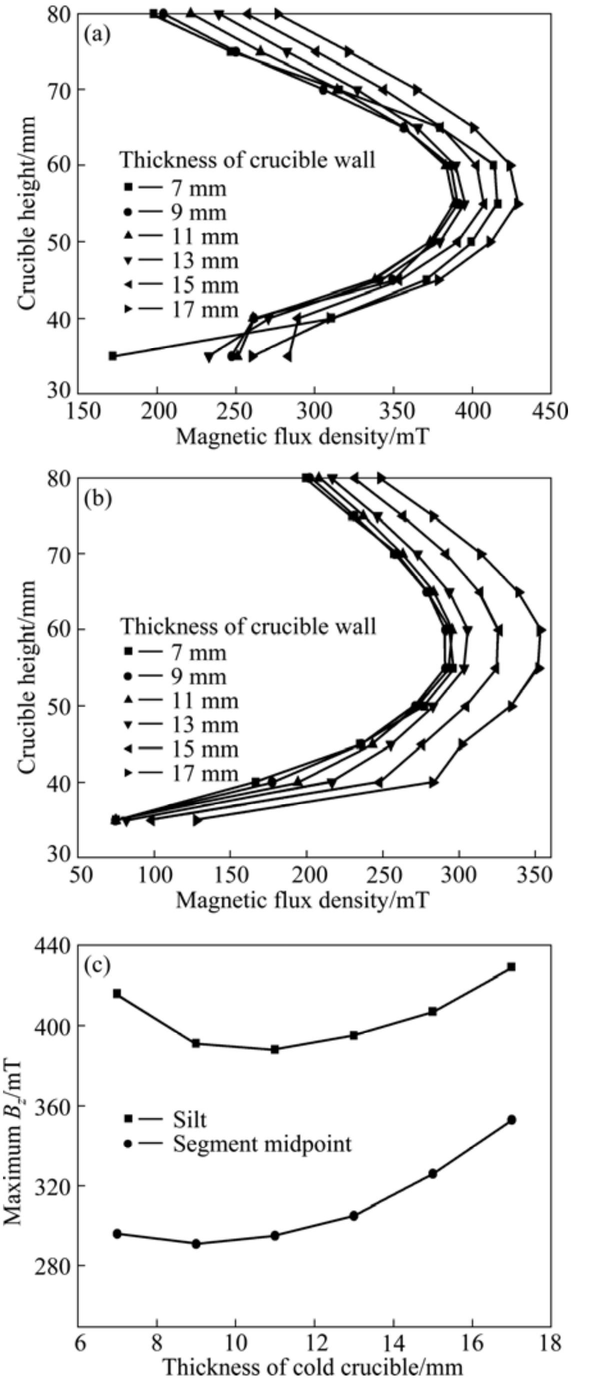

Fig. 5 B_z distribution (a, b) and the maximum B_z (c) under different thicknesses of crucible wall: (a) At slit; (b) At segment midpoint; (c) Maximum B_z

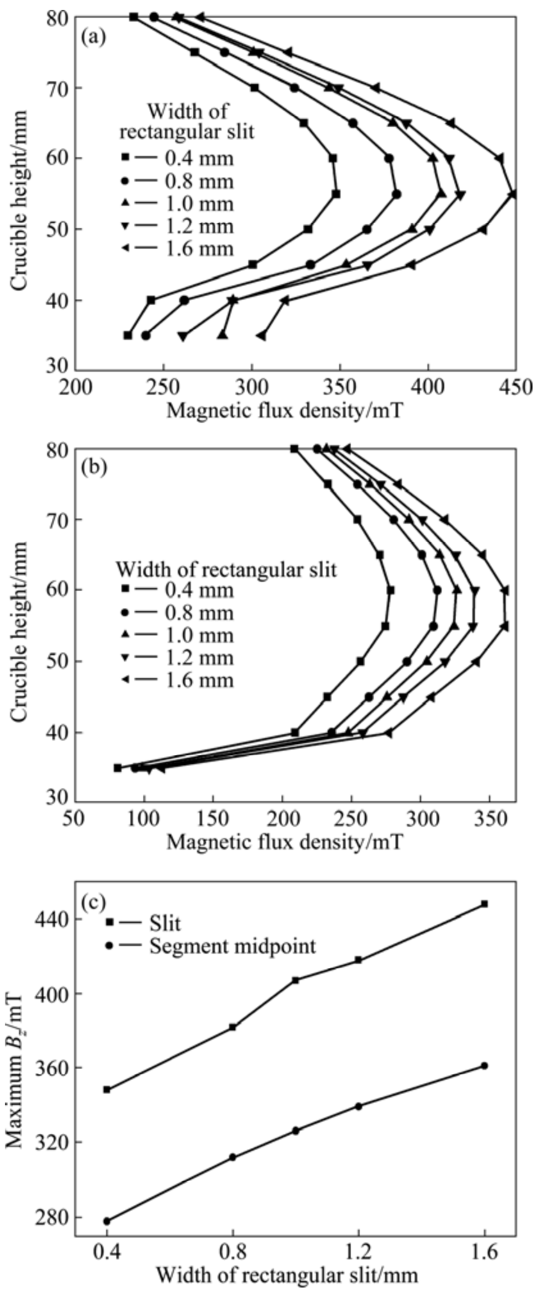

Fig. 6 B_z distribution (a, b) and the maximum B_z (c) under different d: (a) At slit; (b) At segment midpoint; (c) Maximum B_z

3.2.4 Section shape of wedgy slit

The section shape and the geometry dimension of the wedge slit are presented in Fig. 7(a), where W is the variable. With the widening of W from 1 to 15 mm, B_z both at the slit and at the segment midpoint increase; the maximum B_z increases over 25%, which varies from 407 to 532 mT at the slit and from 326 to 406 mT at the segment midpoint, respectively, as illustrated in Figs. 7(b) and (c). FELIACHI et al [14] indicated that the segment with a triangle section shape possesses the best EM transparency, which coincides with the results in this investigation. The curves in Fig. 7(d) show that the

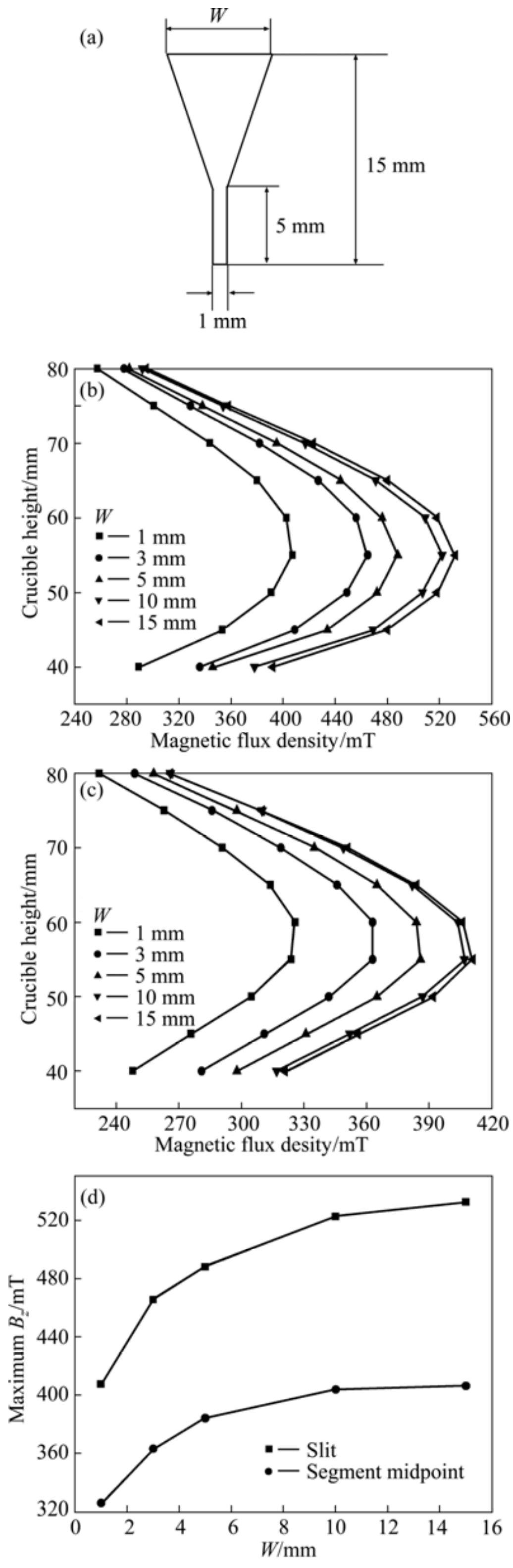

Fig. 7 B_z at different positions under different W: (a) Shape of slit; (b) At slit; (c) At segment midpoint; (d) Maximum B_z

climbing tendency of the maximum B_z gradually slows down with the increase of W. On one hand, the extending section area of the slit improves the crucible transparency. On the other hand, the sharp section shape of the segment is not beneficial to increase of the induced current on the segment regardless of the extending section area of the slit.

Further, the dimension of L is treated as a variable to calculate the magnetic field, as shown in Fig. 8(a). Calculated results reveal that a shorter L is beneficial to enhancing B_z at the slit (Fig. 8(b)) and at the segment midpoint (Fig. 8(c)). Increasing L from 1 to 9 mm will cause the maximum B_z to reduce (Fig. 8(d)), which indicates that a larger area of the slit section can obviously improve the EM transparency. In addition, from the comparison of the curves in Fig. 7(d) and Fig. 8(d), broadening W is a more effective way to improve the EM transparency comparing with shortening L.

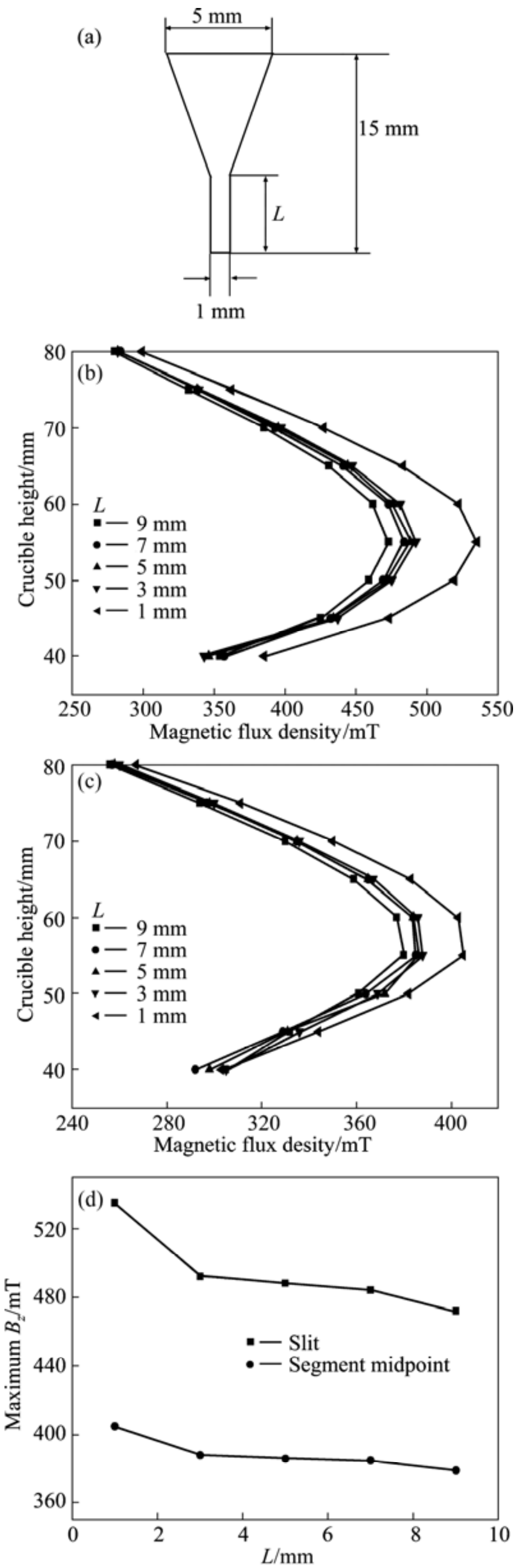

Fig. 8 B_z distribution under different L: (a) Shape of slit; (b) At slit; (c) At segment midpoint; (d) Maximum B_z

3.2.5 Shielding cooper ring

The effects of h_1, h_2 and h_3 are evaluated to explore the influence of the shield ring on the B_z at segment midpoint. The results are shown in Fig. 9. It can be clearly seen form Fig. 9 that the shield ring can strongly impair the B_z, and the B_z will sharply decrease when there is a shield ring close to the induction coil, which can be partly explained by the shielding effect caused by shield ring. Due to a far gap between the induction coil and the upper shield ring, the B_z hardly reduces in the region of the coil.

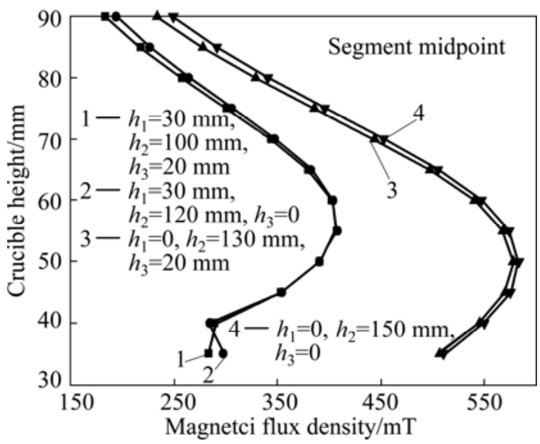

Fig. 9 Effect of shield ring on B_z at segment midpoint

4 Conclusions

1) B_z increases with the decrease of inner diameter and the extending of the slit width in the height range of the induction coil. Under the same height, B_z at the slit is obviously higher than that at the segment midpoint.

2) The maximum B_z decreases initially till reaching the minimum value, and then increases with the increase of the wall thickness.

3) For the wedge slit, broadening W is a more effectively way to improve B_z comparing with shortening L.

4) A shield ring close to the induction coil will strongly decrease B_z in the cold crucible.

Appendix

B — Magnetic flux density (T);

B_z — Magnetic flux density in z direction (T);

μ — Permeability (H/m);
∇ — Hamiltonian operator;
H — Magnetic field strength (A/m);
J — Current density (A/m^2);
E — Electric field strength (V/m);
t — Time (s);
A — Magnetic vector potential (Wb/m);
Φ — Scalar potential (V);
Φ_m — Magnetic scalar potential (A);
ε — Permittivity (F/m);
ρ — Charge density (C/m^3).

References

[1] DING Hong-sheng, CHEN Rui-run, GUO Jing-jie, BI Wei-sheng, XU Da-ming, FU Heng-zhi. Directional solidification of titanium alloys by electromagnetic confinement in cold crucible [J]. Materials Letters, 2005, 59(7): 741−745.

[2] FU Heng-zhi, DING Hong-sheng, CHEN Rui-run, BI Wei-sheng, WANG Yan-li, BAI Yun-feng, XU Da-ming, SU Yan-qing, GUO Jing-jie. Directional solidification technology based on electromagnetic cold crucible to prepare TiAl intermetallics [J]. Rare Metal Materials and Engineering, 2008, 37(4): 565−570. (in Chinese)

[3] CHEN Rui-run, DING Hong-sheng, GUO Jing-jie, BI Wei-sheng, FU Heng-zhi. Continuous and directional solidification technology of titanium alloys with cold crucible [J]. Transactions of Nonferrous Metals Society of China, 2006, 16(s): s154−s159.

[4] DENG Kang, ZHOU Yue-ming, REN Zhong-ming, GONG Tao, JIANG Guo-chang. Electromagnetic characteristics of levitation melting with cold crucible [J]. Transactions of Nonferrous Metals Society of China. 1999, 9(2): 387−392.

[5] WESTPHAL E, MUIZNIEKS A, MUHLBAUER A. Electromagnetic field distribution in an induction furnace with cold crucible [J]. IEEE Transactions on Magnetics, 1996, 32(3): 1601−1604.

[6] GROSS C, ASSMUS W, MUIZNIEKS A, RAMING G, MUKGKBAYER A, STENZEL C. Power consumption of skull melting, part I: Analytical aspects and experiments [J]. Crystal Research and Technology, 1999, 34(3): 319−328.

[7] KAWASE Y, YOSHIDA T. 3-D finite element analysis of molten metal shape in rectangular cold crucible system [J]. IEEE Transactions on Magnetics, 1999, 35(3): 1889−1892.

[8] ZHANG Hai-tao, CUI Jian-zhong. Production of super-high strength aluminum alloy billets by low frequency electromagnetic casting [J]. Transactions of Nonferrous Metals Society of China, 2011, 21(10): 2134−2139.

[9] TANG Meng-ou, XU Jun, ZHANG Zhi-feng, BAI Yue-long. Effects of annulus gap on flow and temperature field in electromagnetic direct chill casting process [J]. Transactions of Nonferrous Metals Society of China, 2011, 21(5): 1123−1129.

[10] CHA P R, HWANG Y S, OH Y J, CHUNG S H, YOON J K. Numerical analysis on cold crucible using 3D H-phi method and finite volume method with non-staggered BFC grid system [J]. ISIJ International, 1996, 36(9): 1157−1165.

[11] CHO Y W, OH Y J, YI K W, CHUNGS H, SHIM J D. Numerical analysis of molten metal shape in cold crucibles by 3D FEM [J]. Modelling and Simulation in Materials Science and Engineering, 1996, 4(1): 11−22.

[12] CHA P R, HWANG Y S, NAM H S, CHUNG S H, YOON J K. 3D numerical analysis on electromagnetic and fluid dynamic phenomena in a soft contact electromagnetic slab caster [J]. ISIJ International, 1998, 38(5): 403−410.

[13] WESTPHAL E, MUIZNIEKS A, MUHLBAUER A. Electromagnetic field distribution in an induction furnace with cold crucible [J]. IEEE Transactions on Magnetics, 1996, 32(3): 1601−1604.

[14] FELIACHI M, BENZERGA D, LOUAI F Z M, DEVELEY G. On the 2D or 3D coupled analytical and finite element analysis of eddy current and thermal problems in plasma devices [J]. IEEE Transactions on Magnetics, 1996, 32(3): 1613−1616.

[15] JIAO Qi-xiang. Electromagnetic field and electromagnetic wave [M]. Beijing: Science Press, 2010: 200−209. (in Chinese)

[16] XIE De-xin, YANG Shi-you. Analysis and synthesis of engineering electromagnetic field [M]. Beijing: China Machine Press, 2009: 56. (in Chinese)

[17] CHEN Rui-run, YANG Jie-ren, DING Hong-sheng, HUANG Feng, SU Yan-qing, GUO Jing-jie, FU Heng-zhi. Effect of power parameter and induction coil on the magnetic field in cold crucible during continous melting and directional solidification [J].China Foundry, 2012, 1: 15−19.

结构对连续熔化与定向凝固用冷坩埚磁场的影响

陈瑞润, 杨劼人,丁宏升, 黄 锋, 苏彦庆, 郭景杰, 傅恒志

哈尔滨工业大学 材料科学与工程学院，哈尔滨 150001

摘　要：为了提高连续熔铸与定向凝固用冷坩埚的工作效率和优化结构设计，基于实验验证，建立了不同结构的电磁冷坩埚的 3D 有限元模型，并研究了坩埚结构对其内部磁场的影响规律。电磁冷坩埚的结构变量包括坩埚内径、坩埚壁厚、开缝形状以及水冷铜环。结果表明：随着坩埚内径的减小、开缝宽度和横截面积的增大以及水冷铜环的去除，坩埚内分瓣中点和开缝处的磁场随之增强。此外，当外径一定时，存在一个最差的坩埚壁厚使得坩埚内磁场值最低。

关键词：冷坩埚；磁感应强度；结构设计；定向凝固

(Edited by LI Xiang-qun)